An Interstellar Conduction Front Within a Wolf-Rayet Ring Nebula Observed with the GHRS

Bram Boroson[1], Richard McCray, and Christina Oelfke Clark

JILA, Campus Box 440, University of Colorado, Boulder, CO 80309;

boroson@head-cfa.harvard.edu, dick@jila.colorado.edu, oelfke@ucsu.colorado.edu

Jonathan Slavin

NASA/Goddard Space Flight Center, Code 685, Greenbelt, MD 20771;

slavin@shock.gsfc.nasa.gov

Mordecai-Mark Mac Low

Max-Planck-Institut für Astronomie, Königstuhl 17, 69117 Heidelberg, Germany;

mordecai@mpia-hd.mpg.de

You-Hua Chu

Astronomy Dept., University of Illinois, Urbana, IL 61801; chu@astro.uiuc.edu

and

Dave Van Buren

Infrared Processing and Analysis Center, California Institute of Technology, Pasadena, CA 91125; dave@ipac.caltech.edu

Received ______________________; accepted ______________________

[1]Center for Astrophysics, 60 Garden Street, Cambridge, MA 02138

ABSTRACT

With the High Resolution Spectrograph aboard the Hubble Space Telescope we obtained high signal-to-noise ($S/N \gtrsim 200 - 600$ per 17 km s^{-1} resolution element) spectra of narrow absorption lines toward the Wolf-Rayet star HD 50896. The ring nebula S308 that surrounds this star is thought to be caused by a pressure-driven bubble bounded by circumstellar gas (most likely from a red supergiant or luminous blue variable progenitor) pushed aside by a strong stellar wind. Our observation has shown for the first time that blueshifted ($\approx$70 km s^{-1} relative to the star) absorption components of C IV and N V arise in a conduction front between the hot interior of the bubble and the cold shell of swept-up material. These lines set limits on models of the conduction front. Nitrogen in the shell appears to be overabundant by a factor 10.

The P Cygni profiles of N V and C IV are variable, possibly due to a suspected binary companion to HD 50896.

Subject headings: ISM: bubbles, stars: individual (HD 50896), stars: Wolf-Rayet

1. Introduction

About 30% of all Wolf-Rayet (WR) stars are surrounded by ring nebulae (Lozinskaya 1992). The strong stellar winds of these stars ($\dot{M} \sim 10^{-5} M_{\odot}$ yr^{-1}, $V_{\rm wind} \sim 2000$ km s^{-1}) may create the shells by sweeping up interstellar material (Johnson & Hogg 1965) or mass lost by the star during previous stages of evolution (Bisnovatyi-Kogan & Nadezhin 1972; Massevich, Tutukov, & Yungelson 1975). The theory of expanding interstellar bubbles powered by stellar winds (Castor, McCray & Weaver 1975) correctly predicted that bubbles would be weak X-ray sources and would show blueshifted absorption lines in their UV spectra. The dynamical properties of these nebulae have also thus far been roughly consistent with the theory. Weaver et al. (1977) refined the theory to include the nonstationary ionization balance in a radiatively cooling conduction front between the hot interior of the bubble and the cold swept-up shell.

The exchange of mass and energy through conductive interfaces helps to determine the global physical structure of the interstellar medium (ISM; McKee & Ostriker 1977). However, it is difficult to study these interfaces directly, since we do not know their exact locations and physical parameters. As we show here, a Wolf-Rayet ring nebula is an ideal laboratory for studying conductive interfaces in the ISM.

There is substantial evidence that in many WR ring nebulae, the wind does not expand into a uniform medium as assumed (Chu 1983). For example, NGC 6888 is elliptical in shape and anomalously faint in X-rays (Bochkarev 1988; Wrigge, Wendker, & Wisotzki 1994). RCW 58 contains clumps and filaments (Chu 1982; Smith et al. 1988; Chu 1988), and UV absorption lines are blueshifted depending on ionization potential, evidence that cold clumps of ejecta are evaporating in the hot wind (Smith et al. 1984).

Therefore, to better understand the physics of conduction fronts, we observed narrow C IV and N V absorption lines in the spectrum of the bright ($V \approx 6.9$) central WN5 star

HD 50896 (EZ Canis Majoris) of the Sharpless 308 ring nebula. In contrast to many of these nebulae, the S 308 ring nebula appears smooth and nearly spherical (Chu et al. 1982). The N V line should be an excellent diagnostic of the conduction front, since photoionization by the central star should produce little of this ion (Esteban et al. 1993).

We required UV spectra with a high enough signal-to-noise ratio to detect the weak (equivalent width $\sim$5 mÅ) absorption lines that we predicted would arise in the conduction front. With the Goddard High Resolution Spectrograph (GHRS) aboard the Hubble Space Telescope, we achieved spectra of this quality. They show that the N V absorption from the S 308 bubble is substantial.

2. Observations

The observations took place April 10, 1993 (before the HST servicing mission). We used the medium resolution G160M grating with the Large Science Aperture (2" slit), centered on 1240 Å (for the N V doublet) and 1550 Å (for the C IV doublet). The G160M grating has a spectral range of 35 Å and resolution of $R \approx 20,000$.

We expected a count rate high enough that the nonuniformity ("granularity") in the photocathode detectors would be a major source of error (Gilliland et al. 1992, Lambert et al. 1994). To alleviate this problem, we used the "FP-SPLIT" method, which shifts the spectra four times for each exposure. In addition, we took three equal subexposures at each line (though two of the N V exposures were at the same central wavelength). We used these shifted spectra to solve for the photocathode granularity (real features would not shift in wavelength). Since the sensitivity has an rms variation of ~0.5% per diode (~15 km s^{-1}), the error due to granularity should be $\lesssim$ 0.2% merely from the addition of errors, without considering the solutions for the sensitivity. Our solution for the granularity implied a formal error of ~10^{-4} in each diode.

The N V line peaked at 1.3×10^6 counts per diode, for a signal-to-noise (due to counting statistics) ratio of ~10^3 in each 17 km s^{-1} diode. The C IV line peaked at 2.4×10^5 counts diode^{-1}, for a formal S/N ratio of ~500. We believe that when errors of granularity and counting statistics are included, our final S/N ratio is ~200–600 in each diode throughout most of the wavelength range observed.

We recalibrated our wavelength scale by using the "global wavelength solution" (Soderblom, Sherbert & Hulbert 1993). The additional wavelength correction implied by the "Spectrum Y Balance", or SPYBAL exposure (Soderblom, Sherbert & Hulbert 1994) was small, approximately 2 km s^{-1}. We then derived a wavelength scale for each of our 24 exposures. We did not, however, combine the spectra according to these wavelength scales, but correlated features between the spectra. The wavelength shifts at which the spectra were best correlated implied an error of ∼7–8 km s^{-1} in the global wavelength solutions.

Howarth & Schmutz (1995) determined the velocity of Na I optical absorption lines towards HD 50896 from very high resolution spectra ($R \approx 10^5$). We assume that the absorption from low ionization stages seen in our spectra (Mg II, S II, C I) should coincide in velocity with the Na I absorption lines. The exposures in the region of the C IV lines include C I/C I*/C I** absorption at ∼1560 Å at velocities consistent with the velocity shift of the Na I lines. However, the absorption lines in the region of 1240 Å are all blueshifted by ∼15 km s^{-1} from the expected velocities. This finding applies both to the low-velocity, low-ionization lines (Mg II and S II), which are shifted relative to the Na I lines, and also to the N V absorption (which we attribute to the interstellar bubble S 308), which is shifted by ∼15 km s^{-1} from the [O III] emission seen by Chu et al. (1982). There is a 3 km s^{-1} difference between the S II and Mg II velocities; we have set our calibration so that the Na I absorption would fall between the Mg II and S II velocities.

Although the calibration shift of 15 km s^{-1} is greater than the error expected from the variability among our separate wavelength solutions, the resulting agreement of velocities among all low-ionization species and between the N V absorption and the [O III] emission leads us to add 15 km s^{-1} to all velocities in our exposure in the range of 1240 Å.

The exposures centered on 1240 Å lasted 27.2 min., whereas the 1550 Å exposures lasted 16.3 min. The spectra (shown in Fig. 1) are of much higher quality than those obtained with Copernicus (Shull 1977) and IUE (Howarth & Phillips 1986; Nichols-Bohlin & Fesen 1986; Smith, Willis, & Wilson 1980). The spectra of Howarth & Phillips (1986), with a signal to noise ratio of ∼50–75, were the best prior to our observation. In addition to the absorption lines of N V and C IV, we also see Mg II$\lambda\lambda$1239,1240, S II$\lambda\lambda$1250,1253, and C I/C I*/C I**$\lambda\lambda\lambda$1560,1560.7,1563. Equivalent widths and Local Standard of Rest velocities are listed in Table 1 for low-velocity features (and blended features), and in Table 2 for high-velocity features ($V_{\rm LSR} = V_{\rm hel} - 19.5$ km s^{-1}).

Tables 1 and 2 also display results from the literature for a variety of UV absorption lines. Use of both LSR and heliocentric velocities has made comparisons of published values difficult. Also, absolute wavelength calibration has not been reliable; for this reason, some papers list all velocities relative to the low-velocity component. Following the suggestion of Howarth & Schmutz (1995), we have added +39 km s^{-1} to the IUE-determined velocities of Howarth & Phillips (1986) to convert them to heliocentric velocities. We recalibrated with recent and accurate rest wavelength determinations (Verner, Barthel, & Tytler 1994).

By employing deconvolution techniques (Lucy 1974; Jansson 1984), we can improve spectral resolution at the cost of increasing the noise. In Figure 2 we display spectra deconvolved by using the slightly superior Jansson technique applied to data presmoothed with a Wiener filter.

The C IV and N V lines are doublets. Since the blue components have twice the oscillator strength of the red components, the optical depths in the absorption lines should also have the expected 2:1 ratio for all velocities. Figure 3 shows the optical depth as a function of velocity, $\tau(v)$, in the deconvolved spectra. The two components $\tau_{\rm blue}(v)$ and $2\tau_{\rm red}(v)$ can be compared to give a rough estimate of our total error. To find τ, we fit several overlapping parts of the spectrum with polynomials, excluding the regions contaminated by lines. We assume that these polynomials represent the unabsorbed continuum. Where the absorption is saturated, we cannot accurately measure τ, and here the less saturated line $\tau_{\rm red}$ provides a better estimate. While the N V and Mg II lines are shallow and unsaturated, the S II and C IV lines become saturated toward line center, and depart from a 2:1 ratio of $\tau_{\rm blue}$ to $\tau_{\rm red}$. We suspect that the saturation of these lines leads to an underestimate of the optical depths, especially in the blue components.

Figure 4 shows the ratio of the optical depths in the C IV and N V lines. Near the centers of the lines, the ratios for the two doublet components disagree because of the saturation of C IV. (The red components suffer less from saturation and are probably more accurate.) If we had not made the 15 km s^{-1} shift in the exposure containing the N V lines, then N V would be overabundant at a blue shift of $\sim$60 km s^{-1} LSR.

Figure 5 shows a schematic view of the velocities of the absorption lines observed with the *GHRS*, the velocity shifts we have made, and the velocities attributed to HD 50896, the expanding shell of S 308, and a putative supernova remnant (Nichols-Bohlin & Fesen 1986) from observations at other wavelengths.

3. Results and Interpretations

3.1. The Conduction Front in S 308

Because radiative cooling peaks at a temperature $T \approx 10^5$K, interstellar gas is expected to be predominantly hot ($T \approx 10^7 - 10^8$K, McCray 1987) or cool ($T \approx 10^4$K). At the interfaces between interstellar gas at these stable temperatures, thermal conduction will evaporate cold material into a warm transition region of $T \approx 10^5$ K, ideal for the formation of O VI, N V, and C IV (Cowie & McKee 1977; McKee & Cowie 1977; Balbus & McKee 1982). Observations of absorption due to these ions is not conclusive evidence of a conduction front, however, since photionization and shocks can also be present. In the case of S 308, we know the velocity of the expanding shell from optical observations (Chu et al. 1982) and recent ROSAT observations (Wrigge 1996) show the presence of hot gas in the interior. Thus we have a strong expectation for finding a conduction front along the line of sight towards HD 50896.

The argument that the N V absorption arises in a conduction front is bolstered by a comparison of the observed N V absorption with absorption towards other stars with sight-lines that do not intersect known bubbles. From observations with the *GHRS* of interstellar absorption towards 12 stars (Sembach & Savage 1992), we would expect $N(N\,V) \sim 4 \times 10^{12}$ cm^{-2} (assuming for HD 50896 a distance of 2 kpc and a height above the galactic plane of $z \sim$300 pc). This column density is similar to that observed for the low-velocity N V gas ($N(N\,V) \approx 5 \times 10^{12}$ cm^{-2}, see Table 4), but an order of magnitude below that observed for the high-velocity gas. We also note that from the model of interstellar absorption of Sembach & Savage, we would expect a C IV column density of $N(C\,IV) \sim 10^{13}$ cm^{-2}, a factor of ~ 15 below that observed towards HD 50896.

Whether the ring nebula surrounding HD 50896 results from a wind interacting with stellar ejecta or interstellar material, a conduction front should form. To model the column densities of C IV and N V in either case, we used the analytic approximations given by Weaver et al. (1977), scaled according to the abundances appropriate for S 308. That is, the column density of O VI, N(O VI), is given by

$$N(\mathrm{O\,VI}) \approx 5.2 \times 10^{16} X_{\mathrm{O}} n_0^{9/35} L_{36}^{1/35} t_6^{8/35} \mathrm{cm}^{-2}, \tag{1}$$

where X_{O} (given by Weaver et al. as 4.4×10^{-4}) is the fractional abundance of oxygen, n_0 is the ambient proton density, L_{36} is the wind luminosity in units of 10^{36} erg s^{-1} ($L \equiv 1/2\dot{M}V_{\mathrm{w}}^2$), and t_6 is the age of the bubble in 10^6 years. These variables can be reduced to observed quantities through

$$\rho_0 = \frac{125}{154\pi} t^3 L / R_{\mathrm{s}}^5 \tag{2}$$

and

$$t = (3/5) R_{\mathrm{s}} / V_{\mathrm{shell}} \tag{3}$$

where ρ_0 is the mass density, R_{s} is the radius of the shell, and V_{shell} is its velocity. To find column densities of nitrogen and carbon, we use $N(N\,V)/N(O\,VI) = -1.2$ and

$N(C\,IV)/N(O\,VI) = -0.8$, as given in Weaver et al. (1977). We then scaled the resulting column densities according to the abundances given in Table 4.

We find that, in spite of our incomplete knowledge of S 308 and HD 50896, the theory predicts a narrow range of possible column densities for these ions (Table 4). In Table 4, we also display the column densities calculated from the observed equivalent widths (shown in Table 1 and Table 2). We assume the N V lines are on the linear portion of the curve of growth (the equivalent width is proportional to the column density), while we obtain a lower limit for the column density of the C IV lines (which probably contain several components) using the deconvolved line profiles. The saturated C IV absorption lines are far too strong to arise in a conduction front, but probably originate either in another ionization front or as a result of photoionization.

The strong blueshifted absorption component of N V has most recently been attributed to an unobserved supernova remnant along the line of sight to HD 50896 (Howarth & Phillips 1986; Nichols-Bohlin & Fesen 1986). IUE observations of stars within a region of 3° around HD 50896 show blueshifted absorption from low-ionization species at high velocities (Nichols-Bohlin & Fesen 1986; Howarth & Phillips 1986). However, the IUE spectra of stars in this region did not have a high enough S/N to detect high velocity absorption from species such as C IV, Si IV, and N V at column densities similar to those observed in HD 50896. Furthermore, redshifted absorption corresponding to the receding hemisphere of the shell has not been observed, although this does not rule out an origin in a SNR (Nichols-Bohlin & Fesen 1986).

Both the putative SNR and the ring nebula S 308 expand at velocities near that of the N V absorber. We identify this absorption with the ring nebula and not the SNR because the SNR is not observed at other wavelengths, and only absorption from low ionization species has been seen near -50 km s^{-1} LSR from nearby stars.

Without proper calibration for the IUE velocities, Howarth & Phillips (1986) identified the shallow, low-velocity N V absorption at $\approx$20 km s^{-1} LSR with S 308. However, this velocity is inconsistent with the emission velocity of -40 km s^{-1} LSR seen by Chu et al. (1982) from several lines of sight to S 308. In our model, the strong absorption component arises in a shell expanding at 80 km s^{-1} (the hot gas expands $\sim$5 km s^{-1} slower than the cold edge of the shell). Since the central star has a velocity of +33 km s^{-1} LSR (Chu et al. 1982), we expect to see N V absorption at -42 km s^{-1}. The actual N V absorption appears at -50 km s^{-1}; this velocity difference could be attributed to calibration errors (the alignment of Mg II and S II with the Na I interstellar velocity) or the nitrogen could be moving faster than the [O III] observed by Chu et al. (1982).

The deconvolved S II line profile (Figure 3d) shows weak absorption at -50 km s^{-1} LSR, consistent with an origin in the the same gas as the N V absorber. The equivalent width of the weak S II line implies an absorbing column density of $\log(N) = 13.9 \pm 0.1$ cm^{-2} (Howarth & Phillips give $\log(N) = 13.51 \pm 0.21$). We only see this line in our deconvolved spectra, and the Jansson deconvolution technique may lead to an overestimate of the column density of a weak absorption feature because it forces the flux to be less than the continuum level. The presence of S II at the same velocity as N V suggests that the gas at -50 km s^{-1} LSR contains several temperature zones. This would be expected to occur in both a SNR shock front and in the conductive interface between a cold shell (containing S II) and the hot interior of S 308.

We considered a range of models to fit the data (Table 4). We adopt Model E as the most likely set of parameters for HD 50896/S 308. This model assumes that HD 50896 is distant ($D = 2$ kpc) and that the shell expansion is fast (80 km s^{-1}), and we use the wind speed at which the P Cygni absorption is saturated (1700 km s^{-1}). The N V column density predicted by this model is about a factor of 10 below the observed value. Thus S 308 is probably enriched in nitrogen, as would be expected if the shell is swept-up circumstellar ejecta. While our models A and B agree well with the observed N V column density, we have rejected the identification of the low-velocity absorption with the conduction front because it does not match the expected velocity. We therefore identify the high-velocity N V absorption with a nitrogen-enriched conduction front.

3.2. P Cygni Lines and Variability

The P Cygni line profiles are consistent with the previously reported wind velocity of 1700 km s^{-1} (this is the edge of the saturated absorption; the absorption edge at 2700 km s^{-1} is not typical of most of the wind material). Table 3 contains information on the P Cygni lines during each FP-SPLIT subexposure. The redshifted part of the N V P Cygni profile varied by as much as 5% within 5 min. It would be unusual for a variation this strong to result from calibration problems. If the aperture projection onto the photocathode relative to the diodes drifts vertically due to geomagnetic interference, one might expect to see the spectrum to change with a gradient with wavelength (Gilliland 1994). We examined the change in the spectrum over a 10 minute interval and found that at wavelengths longer than the saturated P Cygni absorption, there was a roughly constant fractional decrease in the flux, while there was a roughly constant fractional increase in the flux at shorter wavelengths. While this might suggest an instrumental problem, it is curious that the spectrum should pivot about a wavelength in the region of saturated P Cygni absorption.

Assuming that the spectral variation is not instrumental, it could be the result of a compact companion to HD 50896 suggested by photometry and polarimetry (a 3.77-day period was found by Drissen et al. 1989, and a possible 0.11 second period was suggested by Marchenko et al. 1994).

We have modeled the N V profile by assuming spherical symmetry and integrating the Sobolev source function exactly (using the SEI method of Lamers et al. 1987, which also allows wind turbulence). A variable X-ray source with X-ray luminosity $L_{\mathrm{X}} \sim 10^{36}$ erg s^{-1} embedded in a stellar wind can produce rapid changes in the P Cygni profiles of ions such as C IV and N V (Kallman, McCray, & Voit 1987; Boroson et al. 1996). However, this model may not apply to HD 50896, for which $L_{\mathrm{X}} \approx 10^{33}$ ergs s^{-1} (Pollock 1987) and the red parts of the N V and C IV profiles are too strong to result entirely from resonance scattering. The emission is provided instead by collisional excitations, which are sensitive to temperature and velocity variations with distance from HD 50896. A small uniform change in the wind temperature (from 60,000 K to 58,500 K) could account for the observed change in the P Cygni line equivalent width.

Though the exact mechanism for the rapid P Cygni profile variability is not yet understood, only a small perturbation of the wind is needed to account for it.

3.3. The Energy Budget Problem of S 308

Van Buren (1986) pointed out that the kinetic energy of the shell S 308 is a fraction $\epsilon_{\mathrm{s}} \approx 0.05$ of the energy deposited by the stellar wind, whereas the theory developed by Weaver et al. (1977) predicts $\epsilon_{\mathrm{s}} = 0.2$. This discrepancy could be resolved if the shell is more massive than Van Buren supposed ($M_{\mathrm{s}} = 220 M_{\odot}$), but this would imply ambient interstellar densities of $n_0 > 4$ cm^{-3}. This is unlikely because HD 50896 is ~300 pc above the galactic plane and may be in the low-density interior of a bubble swept out during earlier stages of the star's evolution.

If S 308 is not of interstellar origin but contains gas supplied by the star itself during a previous stage of mass loss (Garcia-Segura & Mac Low 1995) then the mass implied for S308 by energy considerations ($\sim 400 M_{\odot}$) is more than can reasonably have been supplied by HD 50896 and its possible companion.

The energy budget problem could be solved if the WR wind had a much lower mass-loss rate (several $10^{-6} M_{\odot}$ yr^{-1}) during the dynamical age of the shell ($\approx 10^5$ years). Indeed, determinations of current mass-loss rates for WR stars from radio observations may be in error by a factor of $\gtrsim 3$ if the wind is clumpy (Moffat & Robert 1994). We have theoretical expectations that the mass-loss rates of WR stars are variable (Garcia-Segura, Mc Low, & Langer 1996). The kinetic energy of S 308 should be properly compared not with the current wind luminosity, but with the wind luminosity over the dynamical age of the bubble, which may be much less. In this case, our model predictions of the N V column density in the conduction front (Table 4) should not need to be revised, since the bubble theory (Weaver et al. 1977) predicts $N(N\,V) \sim L^{1/35}$.

We note that a similar energy budget problem for the WR ring nebula NGC 6888 (Garcia-Segura & Mac Low 1995) could be resolved if the WR mass loss rate during the formation of NGC 6888 was also much lower than that inferred at the present epoch.

3.4. Density inferred from C I line ratios

The low-velocity lines of C I,C I*,C I** ($\lambda = 1560, 1560.7, 1563$) provide a useful density diagnostic. The neutral absorption towards HD 50896 has been investigated by Howarth & Schmutz (1995), who resolved separate narrow (< 3 km s^{-1}) components of Na I. From their analysis, we expect the C I absorption to be saturated. In this case, the ratios of the equivalent widths of the C I lines will not suffice to determine electron density.

To estimate a density, we decompose the C I lines into the same components as the Na I low-velocity lines observed by Howarth & Schmutz (1995). Since our data only provide a resolution $R \approx 20,000$, we cannot expect to deduce the density in each individual absorption component; instead we assume that every absorber has the same electron density $n_{\rm e}$.

We model the three C I lines by assuming further that each of the ratios Na I/C I, Na I/C I*, and Na I/C I** has the same value in every absorber. The 90% confidence range in these ratios thus determines the likely range of electron density (there is a weak dependence on temperature and ionization state of the gas). Figure 6 shows the observed C I lines superimposed on the model derived from the Na I lines. We also show the line profile expected after the HRS line spread function is applied.

We include the effects of collisional excitation of C I by protons (Roueff & Bourlot 1990) and neutral hydrogen (Launay & Roueff 1977). For electron impact excitation, we use the results of Johnson, Burke, & Kingston (1987).

The results are shown in Figure 7. Clearly, the values of n_e implied by the separate line ratios (C I*/C I, C I**/C I, and C I*/C I**) are consistent for a wide range of temperatures and degrees of ionization. If the gas containing the C I is largely neutral, then $n_e \gtrsim 100$ cm^{-3}, whereas if the gas is ionized, then $n_e \sim 1$ cm^{-3}. Inferred densities are lower if the gas is hotter.

3.5. Low-velocity Absorption Components

Two observing campaigns have targeted stars in the field of view of HD 50896; Howarth & Phillips (1986) used IUE, and Howarth & Schmutz (1995) observed Na I lines at high resolution. We note that none of the stars observed with IUE showed C IV absorption comparable in equivalent width to that observed towards HD 50896. Among the stars observed by Howarth & Schmutz (1995), only HD 50562 and HD 51854 show absorption as complex as HD 50896, including absorption at $\gtrsim$30 km s^{-1} LSR (we exclude the star -22 1661, which is farther away at $D = 3.4$ kpc). It is likely that the C IV absorption arises in gas surrounding HD 50896. The C IV absorption is redshifted by $\approx$ 18 km s^{-1} from HD 50896; this may represent the expansion speed of a red supergiant or luminous blue variable wind which is being swept up by the bubble and photoionized by the central star.

We note that the Na I spectra of Howarth & Schmutz show absorption at +14.5 km s^{-1} LSR which is seen only in HD 50896 and not in nearby stars. This absorption component may be associated with HD 50896; perhaps not with the nebula S 308 (which expands at a higher velocity), but with the wind of a red supergiant progenitor. The problem with such an interpretation is that the WR star is likely to ionize the circumstellar gas. While the EUV spectrum of HD 50896 and the neutral mass of the shell are both uncertain, Chu et al. (1982) have argued that the nearby H II regions S 303 and S 304 are photoionized by HD 50896. We have also just attributed the C IV absorption to photoionized gas surrounding S 308. From this it would follow that S 308 is density bounded and that circumstellar Na I could only exist in dense clumps. There may be dense neutral clumps of compressed red supergiant wind within S 308, but it is also possible that the structure of neutral absorbers is complex at small scales and the +14.5 km s^{-1} LSR component arises elsewhere.

The low-velocity absorption probably contains unresolved components that arise in physically distinct sources. The relative strengths of these absorption components may be different for each atomic absorber. For example, the strong low-velocity C II absorption seen with IUE is seen in other nearby stars, whereas strong low-velocity C IV absorption is seen only toward HD 50896. It is also possible that the velocities of the Mg II and S II absorption lines, which we have used to calibrate our observation in the region of N V, do *not* match the velocity of the averaged Na I lines. This mismatch could result, for example, if one absorption component is enriched in Mg II or S II, from depletion in grains, or as a result of the different ionization potentials.

3.6. Summary and Future Work

These short exposures with HST (pre-COSTAR) provided spectra with S/N an order of magnitude greater than all the averaged IUE spectra (Howarth & Phillips 1986). We identified absorption lines from the conduction front, compared these absorption lines with the predictions of Weaver et al. (1977), and inferred that the gas is enriched in nitrogen. In addition, we saw variability in the wind of HD 50896 on a very short timescale (<5 min.).

The dynamical evolution of a bubble depends on the amount of energy radiated away in the conduction front. The N V ion may be an important contributor to the energy loss of the bubble. Our observation that this ion is present (and enhanced by a factor of ~ 10) may bear on the question of the future evolution of the bubble. All our models meet the limit set on O VI absorption by *Copernicus* (Shull 1977); even more energy is likely to be radiated away by O VI so future observations of this absorption feature (with FUSE, for example) are likely to be extremely important.

Our observations will constrain models of conductive interfaces that include physical effects we have neglected, such as the saturation of conduction (Cowie & McKee 1977) and the evolution of instabilities in the shell (Garcia-Segura & Mac Low 1994).

Optical observations could determine the density in the shell, and thus its mass. Such data would show whether S 308 is too massive to be of stellar origin. Observations of conduction fronts in similar structures could indicate whether nitrogen enhancement is a common phenomenon. Finally, observations using the Space Telescope Imaging Spectrograph (STIS) should greatly enhance our understanding of ring nebulae around WR stars and conduction fronts in the interstellar medium.

For their advice and assistance, we would like to thank Ron Gilliland, Linda Sherbert, Lauretta Nagel, Rob Fesen, and Ian Howarth.

This work was based on observations with the NASA/ESA Hubble Space Telescope, obtained at the Space Telescope Science Institute, which is operated by the Association of Universities for Research in Astronomy, Inc., under NASA contract NAS 5-26555.

TABLES

Table 1. Low-velocity Lines in HD 50896

Line	λ^{a}	v (LSR)	EW(mÅ)	Ref[b]
C I	1188.833	7.7	11.6	1
	1188.833	-2.6	5.6	1
	1188.833	3.5	20±10	2
	1193.030	25.5	9±8	2
	1260.736	7.5	38.7	1
	1260.736	6.1	13	1
	1260.736	22.8	33±5	2
	1260.736	7.8	37	1
	1261 blend*	16	5± 3	2
	1260.736	26.2	6	2
	1276.482	16.7	7±5	2
	1276.482	10.8	97.6	1
	1277.245	22.5	85±7	2
	1277.513*	25.5	24±4	2
	1279.890*	24.2	12±4	2
	1280.135	27.7	28±5	2
	1328.833	21.0	63±5	2
	1329.101*	26.0	37±4	2
	1329.584**	20.9	10±3	2
	1560.3092	20.5	110	*
	1560.3092	21.5	102±9	2
	1560.69*	22.0	54	*
	1560.69*	40.5	55±6	2
	1561.438*	21.5	10±4	2
	1561.438*	20.5	27	*
	1656.928	21.5	172±13	2
	1656.266	43.5	47±7	2
C II	1334.532	14.5,-62,-115	556±35	2
	1335.703	16.5,-57.5,	191±12	2
C IV	1548.195	15	419±4	*
	1548.195	15	447±31	2
	1550.770	15	337±26	*
	1550.770	17.5	328±3	2

Table 1—Continued

Line	λ[a]	v (LSR)	EW(mÅ)	Ref[b]
N I	1134	+2.9	165	1
	1135	+2.1	187	1
	1200	+1.4	205	1
	1200	+10	198	2
	1200	18.5	207	2
	1201	14.5	174	2
N II	1084	+.3	198	1
	1086	-.6	11.0	1
	1086	-1.4	13.2	1
N V	1238.821	+25	14	*
	1238.821	+27.5	7±6	2
	1242.804	+25	5	*
O I	1039	+4.3	179	1
	1302	15.5	229	2
O VI	1038	?	<44	1
Na I	5890,5896	4.8		3
	5890,5896	8.5		3
	5890,5896	14.5		3
	5890,5896	18.0		3
	5890,5896	22.2		3
	5890,5896	27.1		3
	5890,5896	29.5		3
	5890,5896	32.5		3
Mg II	1239.925	18.3	33±5	*
	1240.395	18.8	17±2	*
	1239.925	18.3	35±9	2
	1240.395	13.5	18±8	2
Al II	1670.787	18,-68,-127	335±23	2
Al III	1854.716	29.5	129± 11	2
	1862.790	16.5	94±10	2

Table 1—Continued

Line	λ[a]	v (LSR)	EW(mÅ)	Ref[b]
Si II	1021	?	168	1
	1190	-.2	200	1
	1193	+1.5	242	1
	1304.372	21.4	174±12	2
	1526.708	25.5	237±17	2
	1808.021	24.1	143±11	2
Si III	1206.51	-5.9	223	1
	1206.51	9.5,-65,-112	398±12	2
Si IV	1393.755	19,-50.4	398±12	2
	1402.770	26,-45	167±13	2
P II	1152.81	22	121±27	2
	1532.51	19.5	7	2
P III	1334.866	13.5	13	2
S I	1807.311	32.6	9±5	2
S II	1250.578	1.3	146	1
	1250.578	21.4	134±10	2
	1250.578	21.5	141±3	*
	1253.805	+1.4	174	1
	1253.805	23.1	140±10	2
	1253.805	21.9	173±4	*
	1259.518	0.6	185	1
	1259.518	27	154	2
S III	1013	+1.4	104	1
	1190	+.1	96	1
S IV	1063	+8.1	45	1
Cl I	1347.24	23.5	19±4	2
Cl II	1071	+.3	13.9	1
Ar I	1048	+5.9	156	1
	1067	+4	144	1

Table 1—Continued

Line	λ[a]	v (LSR)	EW(mÅ)	Ref[b]
Ca II	3933.663	33	200±15	2
	3968.468	33.3	120±40	2
V III	1153.179	6.2	35±26	2
	1169.262	47	15±10	2
Mn II	1197.184	11	22±6	2
	1201.118	17.5	10±5	2
Fe II	1055	+1.7	37	1
	1097	-1.6	87	1
	1145	0.0	151	1
Ni II	1317.217	21	25±4	2
	1370.132	25.6	26±5	2
	1454.842	15	7±4	2
	1741.549	18	24±4	2
	1751	12.6	24±6	2
Ge II	1237.0589	17	25±9	4

[a]An asterisk in the "λ" column indicates absorption from an excited level.

[b] References: 1—Shull (1977), 2—Howarth & Phillips (1986), 3—Howarth & Schmutz (1995), *—This work

Table 2. High-velocity lines in HD 50896

Line	λ [a]	v (LSR)	EW (mÅ)	Ref[b]
C II	1334.532	-62,-115	556	2
C II*	1335.703	-58	191	2
C IV	1548.195	-21-110	447±21	2
	1550.770	-30-111	337	2
N I	1134.66	?	<5.8	1
	1134.66	-73.3	17.2	1
	1199.55	-65	60±7	2
	1200.223	-61	43±6	2
	1200	-75.1	44	1
	1200	-76.9	56	1
N II	1083.994	-76.3	85.2	1
	1083.994	-77.7	84.2	1
	1083.994	-84.1	108	1
N II*	1084.575	-81	0.9	1
N V	1238.821	-53	44±9	2
	1238.821	-50, total blend	66±3	*
	1242.804	-61	22±7	2
	1242.804	-50, total blend	32±2	*
O I	1039.23	-73.9	58.6	1
	1302.1685	-77.9	100	1
	1302.1685	-63	125±9	2
Al II	1670.7874	-81	76	1
	1670.7874	-68-127	335±23	2

Table 2—Continued

Line	λ [a]	v (LSR)	EW (mÅ)	Ref[b]
Si II	1190.4158	-71.6	113	1
	1190.4158	-9-52	350±26	2
	1193.2897	-71.6	137	1
	1193.2897	-72.6	151	1
	1193.2897	-74.6	139	1
	1193.2897	+19.5-56	410±30	2
	1260.4221	+24-64	295±10	2
	1304.3702	-81.6	63	1
	1304.3702	-61	68±7	2
	1526.7066	-50.5	112±12	2
Si III	1206.5	-74.3	24	1
	1206.5	-75	33	1
	1206.5	-103	27	1
	1206.5	-64-112	398±12	2
Si IV	1393.755	-18-50	186±13	2
	1403	+26-64	167	2
S II	1250.586	-51	7±2	*
	1253.805	-49	17±3	*
	1259.518	-77.0	8.3	1
	1259.518	-104.6	<2.5	1
	1259.518	-52	7±4	2
S III	1190	-75.6	<3.3	1
Ar I	1048	?	<9.3	1
	1067	?	<8.0	1
Fe II	1055	-81.6	<3.2	1
	1097	-78.6	3.0	1
	1145	-78.6	23.9	1
	1145	-79	21.1	1
	1608	20-50	253±21	2

[a] An asterisk in the "λ" column indicates absorption from an excited level.

[b] References: 1 — Shull (1977), 2 — Howarth & Phillips (1986), 3 — Howarth & Schmutz (1995), 4 — This work

Table 3. Time-variability of P Cygni lines

Observation root name	Start time	End time	EW_{edge}[a]	EW_{abs}	EW_{em}	λ_c[b]
z19d0104t[1]	00:28:38	00:31:00	2.61±0.01	9.41±0.01	-21.78±0.01	1239.02
z19d0104t[2]	00:31:32	00:33:54	2.62	9.43	-21.34	1238.65
z19d0104t[3]	00:34:26	00:36:48	2.67	9.44	-21.10	1238.29
z19d0104t[4]	00:37:20	00:39:42	2.64	9.46	-20.89	1237.92
z19d0105t[1]	00:41:41	00:44:03	2.59	9.43	-21.00	1240.49
z19d0105t[2]	01:33:51	01:36:45	2.61	9.47	-20.18	1240.12
z19d0105t[3]	01:37:17	01:39:39	2.64	9.47	-20.52	1239.76
z19d0105t[4]	01:40:11	01:42:33	2.61	9.48	-20.54	1239.39
z19d0106t[1]	01:44:20	01:46:42	2.58	9.46	-20.56	1240.50
z19d0106t[2]	01:47:14	01:49:37	2.60	9.47	-20.42	1240.14
z19d0106t[3]	01:50:09	01:52:31	2.65	9.50	-20.32	1239.77
z19d0106t[4]	01:53:03	01:55:21	2.62	9.51	-20.11	1239.40
z19d0107t[1]	01:57:08	01:58:35	4.94	9.41	-22.57	1548.37
z19d0107t[2]	01:59:09	02:00:36	4.93	9.44	-21.19	1548.01
z19d0107t[3]	02:01:10	02:02:35	5.00	9.42	-21.84	1547.65
z19d0107t[4]	02:03:11	02:04:34	4.95	9.47	-21.49	1547.3
z19d0108t[1]	02:06:20	02:07:47	4.98	9.45	-21.71	1549.79
z19d0108t[2]	02:08:20	02:09:47	4.96	9.49	-21.27	1549.43
z19d0108t[3]	02:10:20	02:11:47	5.02	9.49	-21.01	1549.08
z19d0108t[4]	02:12:18	02:13:45	4.97	9.51	-20.81	1548.72
z19d0109m[1]	02:15:38	02:17:06	4.98	9.47	-21.34	1551.22
z19d0109m[2]	02:17:38	02:19:06	4.95	9.48	-21.04	1550.86
z19d0109m[3]	02:17:38	02:21:05	5.01	9.48	-20.95	1550.50
z19d0109m[4]	03:11:24	03:12:52	4.94	9.46	-22.26	1550.15

[a]EW_{edge} is the equivalent width of the violet edge of the absorption (all absorption shortward of saturation). The equivalent widths are relative to our choice of continuum and wavelength ranges and show variability in emission with a weaker in absorption.

[b]λ_c is the central wavelength of the exposure.

Table 4. Comparison Between Observed and Modeled Column Densities

Model[a] (Component)	$V_{\rm shell}$[b] ($V_{\rm observed}$)	$v_{\rm wind}$	$D_{\rm kpc}$	$N_{\rm C\,IV}$[c]	$N_{\rm N\,V}$	$N_{\rm O\,VI}$
(High velocity)	$\sim$75				2.5(13)	
(Low velocity)	$\lesssim$40			1.5(14)	5(12)	$<$ 3.5(13)
A	40	1700	2	5.0(12)	4.0(12)	2.5(13)
B	40	2800	2	5.8(12)	4.8(12)	2.9(13)
C	80	1700	2	2.5(12)	2.0(12)	1.2(13)
D	80	2800	2	2.9(12)	2.4(12)	1.4(13)
E	80	1700	1	3.0(12)	2.4(12)	1.4(13)
F	80	2800	1	3.5(12)	2.9(12)	1.7(13)

[a] Notes—For all models, the fractional abundances of carbon, nitrogen, and oxygen are given by $12 + \log_{10} Y_{\rm C} = 8.50$, $12 + \log_{10} Y_{\rm N} = 8.28$, and $12 + \log_{10} Y_{\rm O} = 8.54$. The observationally determined mass-loss rate of HD 50896 has been scaled with distance.

[b] km s^{-1}

[c] cm^{-2}

REFERENCES

Bisnovatyi-Kogan, G. S., & Nadezhin, D. K. Ap&SS, 15, 353.

Bochkarev, N. G. 1988, Nature, 332, 518.

Boroson, B., McCray, R., Kallman, T. R., & Nagase, F. 1996, ApJ, 465, 940.

Castor, J., McCray, R., & Weaver, R. 1975, ApJL, 200, 107.

Chu, Y-H. 1982, ApJ, 254, 578.

Chu, Y-H. 1983, ApJ, 269, 202.

Chu, Y-H. 1988, PASP, 100, 986.

Chu, Y-H., Gull, T.R., Treffers, R. R., Kwitter, K. B., & Troland, T. H. 1982, ApJ, 254, 562.

Cowie, L.L, & McKee, C.F. 1977, ApJ, 211, 135.

Drissen, L., Robert, C. Lamontagne, R., Moffat, A. F. J., St.-Louis, N., van Weeren, N., & van Genderen, A. M. 1989, ApJ 343, 426.

Esteban, C., Smith, L. J., Vilchez, J.M., & Clegg, R. E. S. 1993, A& A, 272, 299.

Garcia-Segura, G., Mac Low, M.-M., & Langer, N. 1996, A& A 305, 229.

Garcia-Segura, G., Mac Low, M.-M. 1994, Proc. 34. Herstmonceux Conf. Circumstellar Media in the Late Stages of Stellar Evolution, ed. R. E. S. Clegg and I. R. Stevens.

Garcia-Segura, G., and Mac Low, M. 1995, ApJ 455, 145.

Gilliland, R.L. 1994, personal communication.

Gilliland, R. L., Morris, S. L., Weymann, R. J., Ebbets, D. C., & Lindler, D. J. 1992, PASP, 104, 367.

Howarth, I. D., & Phillips, A. P. 1986, MNRAS 222, 809.

Howarth, I. D., & Schmutz, W. 1995, A& A 294, 529.

Jansson, P. A. 1984, Deconvolution With Applications in Spectroscopy (New York, Academic).

Johnson, C. T., Burke, P. G., Kingston, A. E. 1987, J. Phys. B., 20, 2553.

Johnson, H. M., & Hogg, D. E. 1965, ApJ 142, 1033.

Kallman, T.R., McCray, R., & Voit, G.M. 1987, ApJ 317, 746.

Lambert, D. L., Sheffer, Y., Gilliland, R. L., Federman, S. R. 1994, ApJ, 420, 756.

Lamers, H. J. G. L. M., Cerruti-Sola, M., Perinotto, M. 1987, ApJ 314, 726.

Launay, M., & Roueff, E. 1977, A& A, 56, 289.

Lozinskaya, T. A. 1992, Supernovae and Stellar Wind in the Interstellar Medium (New York, American Institute of Physics).

Lucy, L. B. 1974, AJ, 79, 745.

Marchenko, S. V., Antokhin, I. I., Bertrand, J.-F., Lamontagne, R., Moffat, A. F. J., Piceno, A., & Matthews, J. M. 1994, AJ, 108, 678.

Massevich, A. G., Tutukov, A. V., and Yungelson, L. R. 1975, Ap&SS, 40, 115.

McCray, R. 1987, in Spectroscopy of Astrophysical Plasmas, p. 255, ed. A. Dalgarno & D. Layzer (Great Britain, Cambridge University Press).

McKee, C.F., & Cowie, L.L. 1977, ApJ, 215, 213.

McKee, C. F. & Ostriker, J. P. 1977, ApJ 218, 148.

Moffat, A.F.J. & Robert, C. 1994, ApJ 421, 310.

Nichols-Bohlin, J., & Fesen, R. A. 1986, AJ, 92, 642.

Pollock, A. M. T. 1987, ApJ 320, 283.

Roueff, E., & Le Bourlot, J. 1990, A& A, 236, 515.

Sembach, K.R. & Savage, B.D. ApJS, 83, 147.

Shull, J. M. 1977, ApJ, 212, 102.

Smith, L. J., Pettini, M., Dyson, J. E., & Hartquist, T. W. 1984, MNRAS 211, 679.

Smith, L. J., Pettini, M., Dyson, J. E., & Hartquist, T. W. 1988, MNRAS, 234, 625.

Smith, L. J., Willis, A. J., & Wilson, R. 1980, MNRAS, 191, 339.

Soderblom, D. R., Sherbert, L. E., & Hulbert, S. J. 1993, in *Calibrating Hubble Space Telescope*, ed. by J. C. Blades and S. J. Osmer (Space Telescope Science Institute, Baltimore), p. 275.

Soderblom, D. R., Sherbert, L. E., & Hulbert, S. J. 1994, *GHRS Instrument Science Report 53*, Space Telescope Science Institute, Baltimore.

van Buren, D. 1986, ApJ, 306, 538.

Verner, D. A., Barthel, P. D., & Tytler, D. 1994, A&AS, 108, 287.

Weaver, R., McCray, R., Castor, J., Shapiro, P., & Moore, R. 1977, ApJ, 218, 377.

Wrigge, M. 1996, A&A submitted.

Wrigge, M., Wendker, H.J., Wisotzki, L. 1994, A&A, 286, 219.

This manuscript was prepared with the AAS LaTeX macros v4.0.

FIGURE CAPTIONS

FIG. 1: *HRS* spectra of HD 50896. In (a), the region around N Vλ1240 is displayed. (b) shows the spectrum near C IVλ1550. Superimposed on the P Cygni lines are the following narrow absorption lines in order of increasing wavelength: (a) N Vλ1238.8 (slope discontinuity in P Cygni profile), Mg II$\lambda\lambda$1238.9,1240.4, N Vλ1242.8, and S II$\lambda\lambda$1250.578,1253.805; (b) C IV$\lambda\lambda$1548.2,1550.77, C I,I*,I**$\lambda\lambda\lambda$1560,1560.3,1560.6.

FIG. 2: The spectra deconvolved with the method of Jansson (1984) and the known pre-COSTAR line spread function of the Large Science Aperture. The smooth curve shows our polynomial fit to the continuum, used to calculate optical depths in the lines and as an upper bound for deconvolution. The raw (shallow absorption) and deconvolved lines are superimposed. In (a), a region around N Vλ1240 is shown; (b) shows a region of C IVλ1550.

FIG. 3: Optical depths $\tau(v)$ determined from doublets. The square and triangle symbols represent, respectively, $\tau_{\rm blue}(v)$ and $2\tau_{\rm red}(v)$. (a)—N V$\lambda\lambda$1238.8, 1242.8, (b)—Mg II$\lambda\lambda$1239.9, 1240.4, (c)–S II$\lambda\lambda$1250, 1253, (d)—C IV$\lambda\lambda$1548.2,1550.8. For plots (a) and (d), we include theoretical profiles from our Model E based on the interstellar bubble theory. We model the data in plots (b) and (c) with a Gaussian with $b = 15$ km s^{-1}.

FIG. 4: The ratio $\tau_{\rm C\,IV}(v)/\tau_{\rm N\,V}(v)$.

FIG. 5: The velocities of the absorption lines observed with the *GHRS*. Towards the top of the panel, we show the velocities of N V, Mg II, S II, C IV, and C I. The N V, Mg II, and S II lines were observed in the same exposure, and have all been given a 15 km s^{-1} shift, as discussed in the text. The velocities of these lines are marked with vertical lines which extend slightly further towards the top of the panel than the C IV and C I lines, which extend slightly further towards the bottom of the panel. In the lower region of the panel, we show the velocities expected for HD 50896, the expansion of S 308, and a putative

SNR along the line of sight.

FIG. 6: The dotted curve shows the C I, C I*, and C I** lines observed by the HRS. The jagged solid curve shows our model based on the Na I absorption components previously observed at higher resolution, and the shallow solid curve shows the model convolved with the HRS line spread function.

FIG. 7: Electron density versus temperature, deduced from the C I, C I*, C I** lines. The solid lines show the 90% confidence interval of electron density implied by the C I*/C I ratio, the dashed line shows the result for the C I**/C I ratio, and the dotted and dashed line shows the result for the C I**/C I* ratio.

4. FIGURES

Figure 1

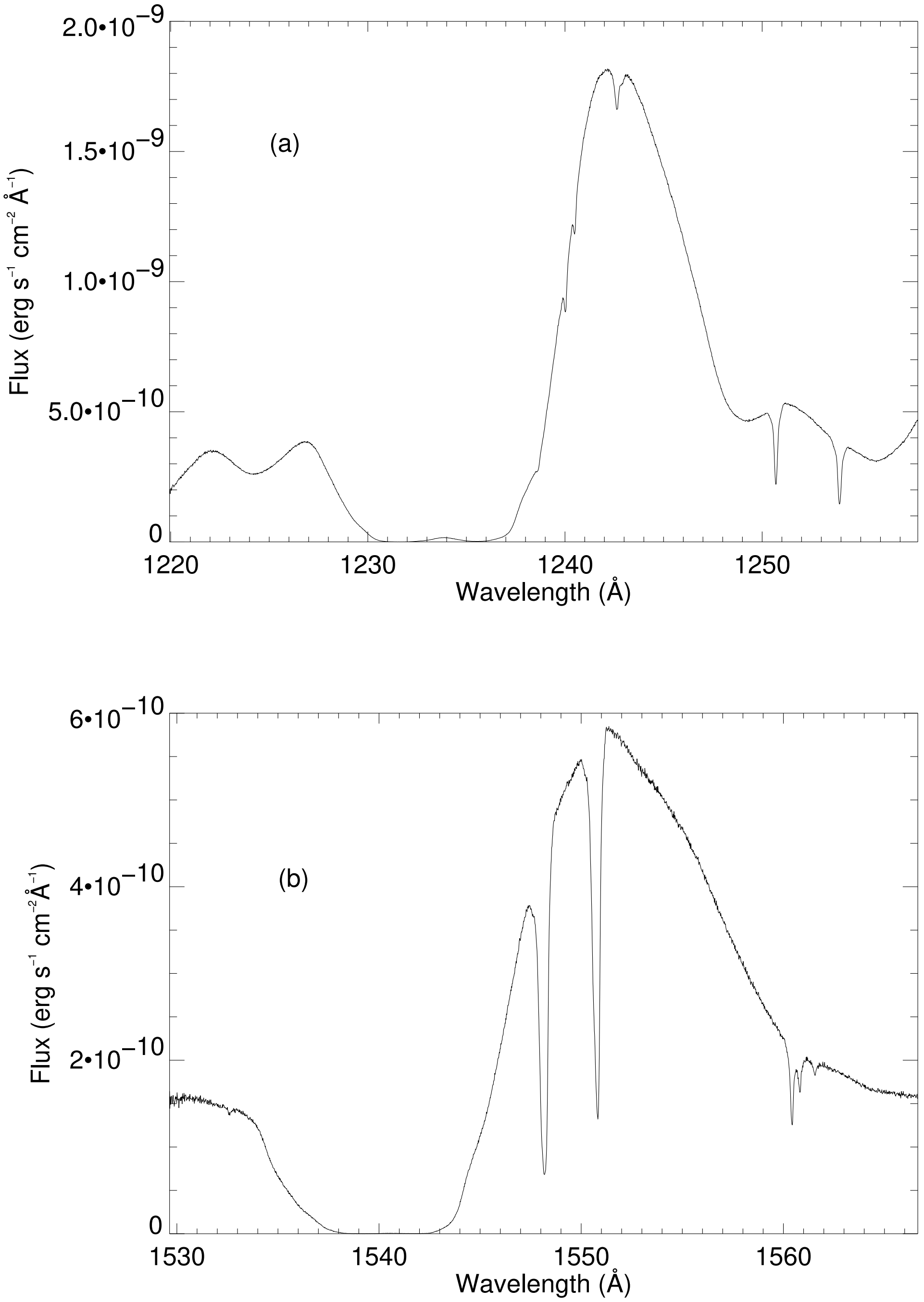

Figure 2

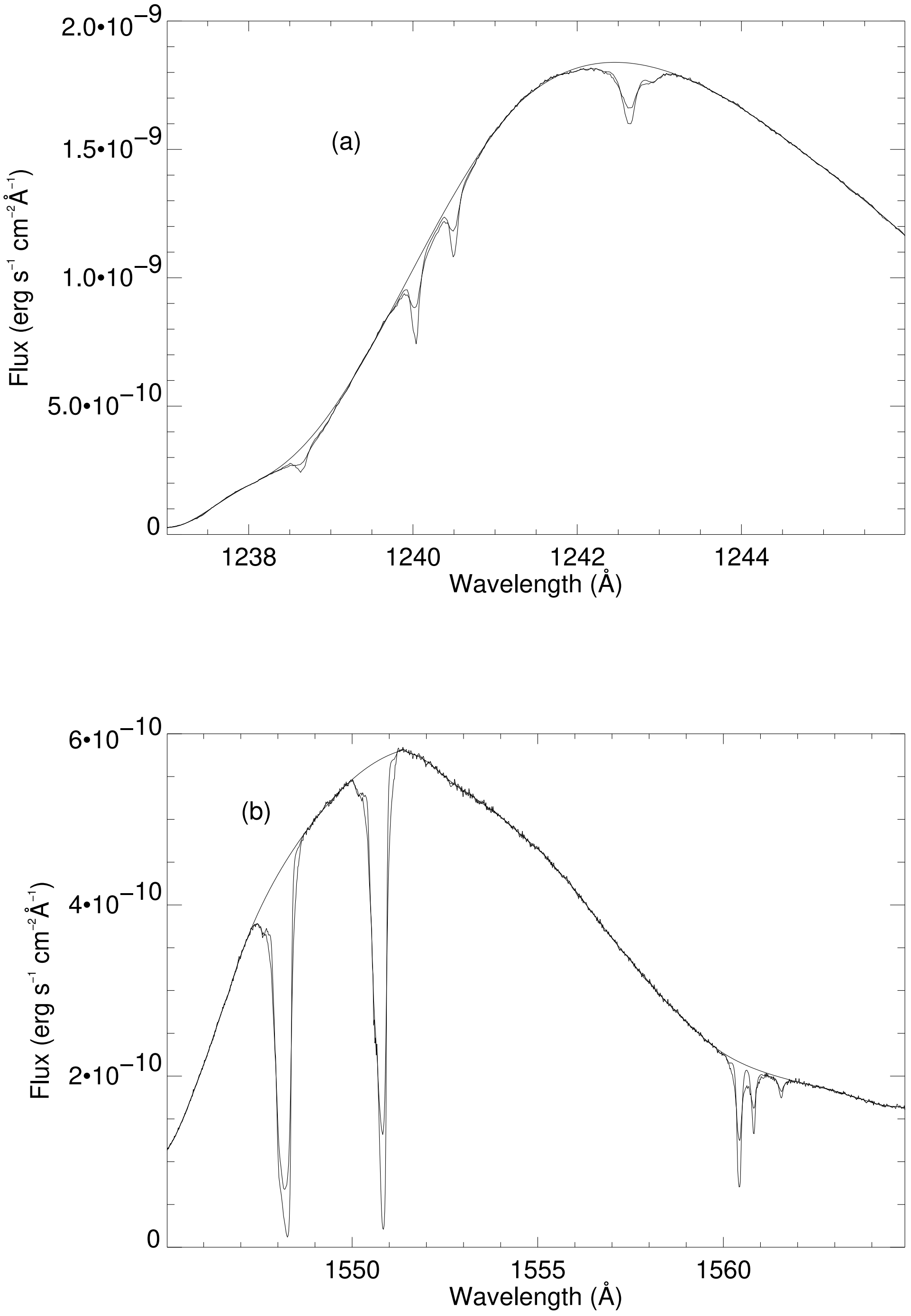
(a)
Flux (erg s^{-1} cm^{-2}Å^{-1})
2.0•10^{-9}
1.5•10^{-9}
1.0•10^{-9}
5.0•10^{-10}
0
1238
1240
1242
1244
Wavelength (Å)
(b)
Flux (erg s^{-1} cm^{-2}Å^{-1})
6•10^{-10}
4•10^{-10}
2•10^{-10}
0
1550
1555
1560
Wavelength (Å)

Figure 3

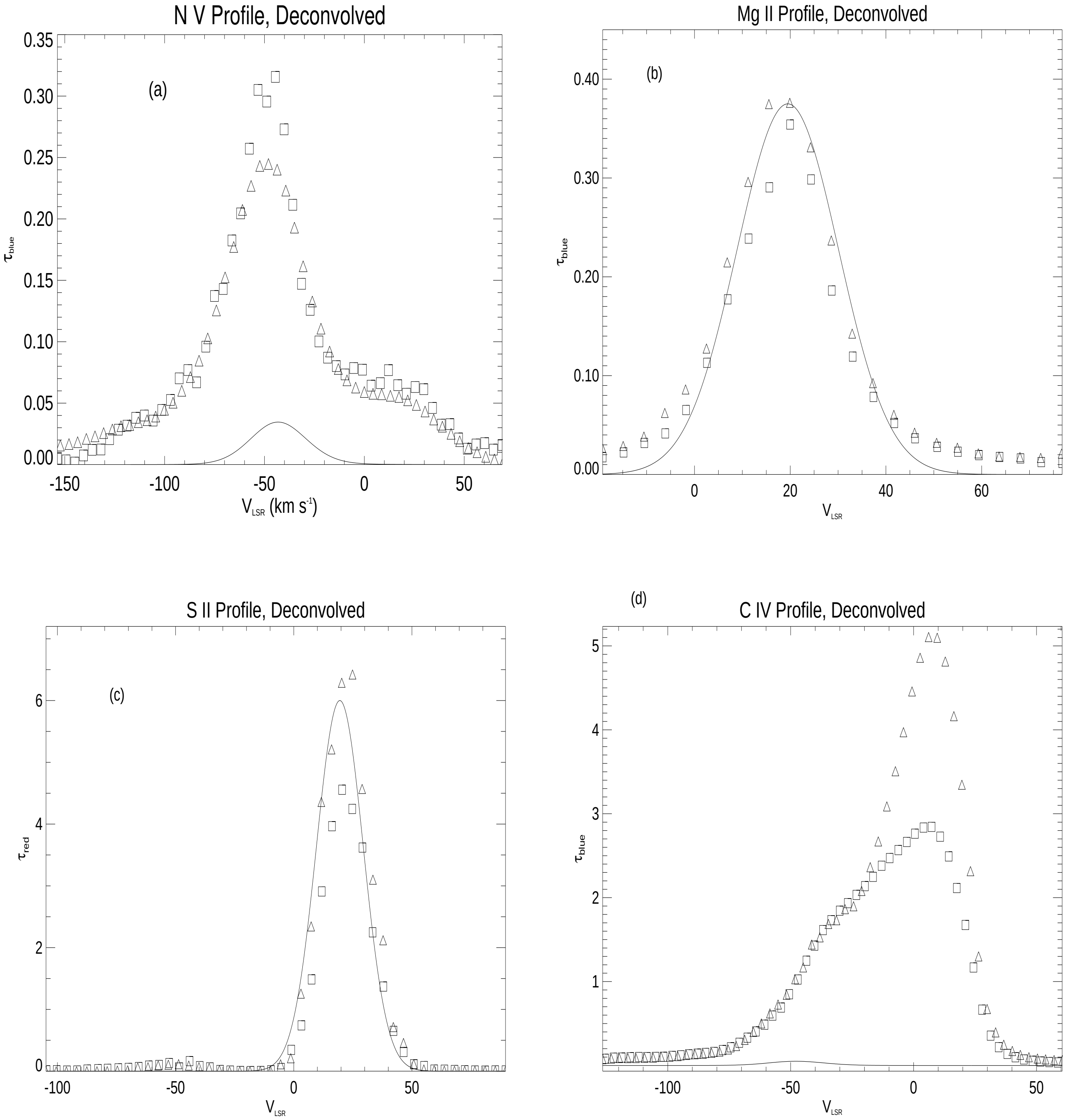
N V Profile, Deconvolved
(a)
τ_{blue}
V_{LSR} (km s^{-1})
Mg II Profile, Deconvolved
(b)
τ_{blue}
V_{LSR}
S II Profile, Deconvolved
(c)
τ_{red}
V_{LSR}
(d)
C IV Profile, Deconvolved
τ_{blue}
V_{LSR}

Figure 4

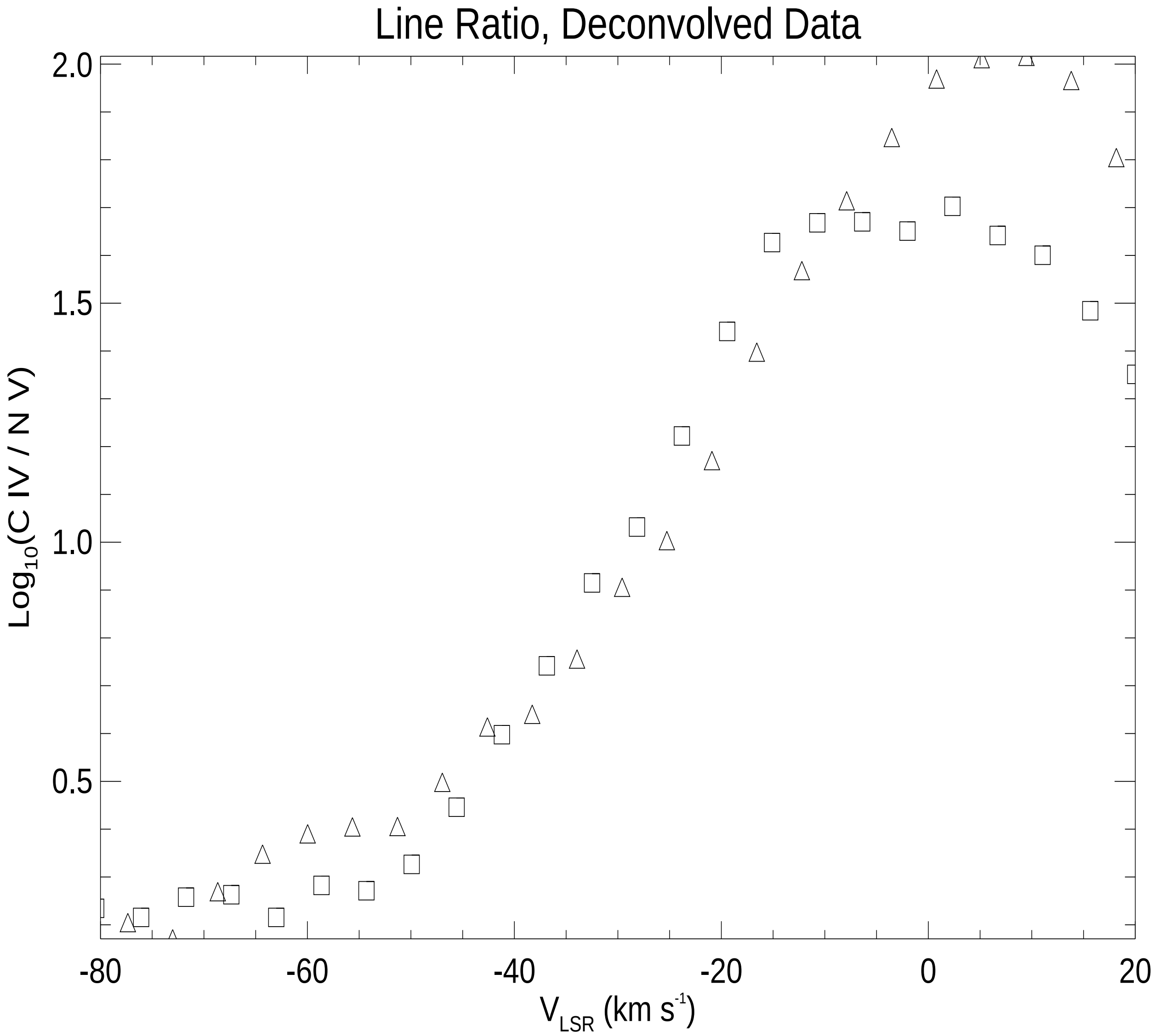
Line Ratio, Deconvolved Data
2.0
1.5
1.0
0.5
Log10(C IV / N V)
-80
-60
-40
-20
0
20
VLSR (km s-1)

Figure 5

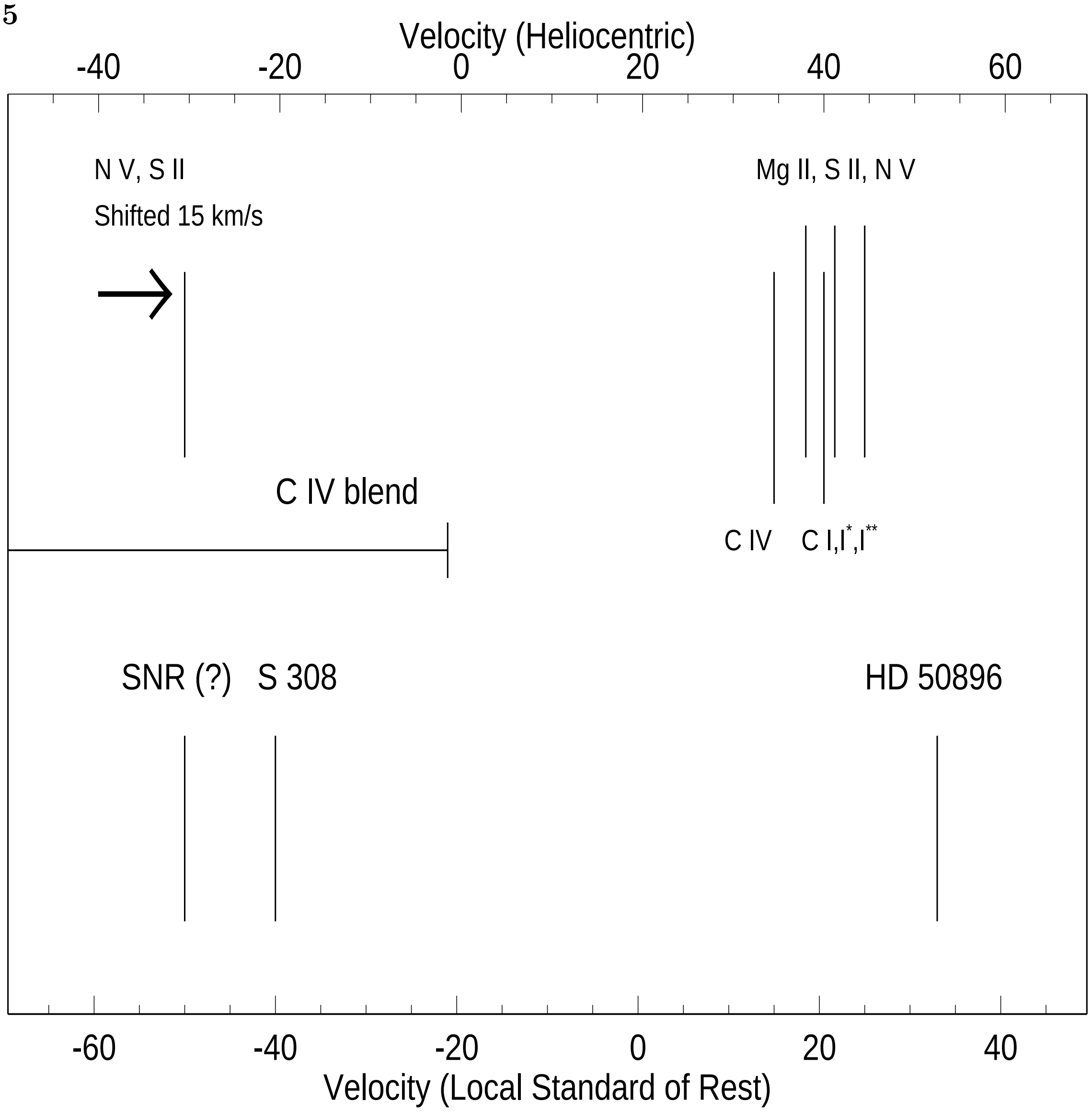
Velocity (Heliocentric)
-40
-20
0
20
40
60
N V, S II
Shifted 15 km/s
Mg II, S II, N V
C IV blend
C IV
C I,I*,I**
SNR (?)
S 308
HD 50896
-60
-40
-20
0
20
40
Velocity (Local Standard of Rest)

Figure 6

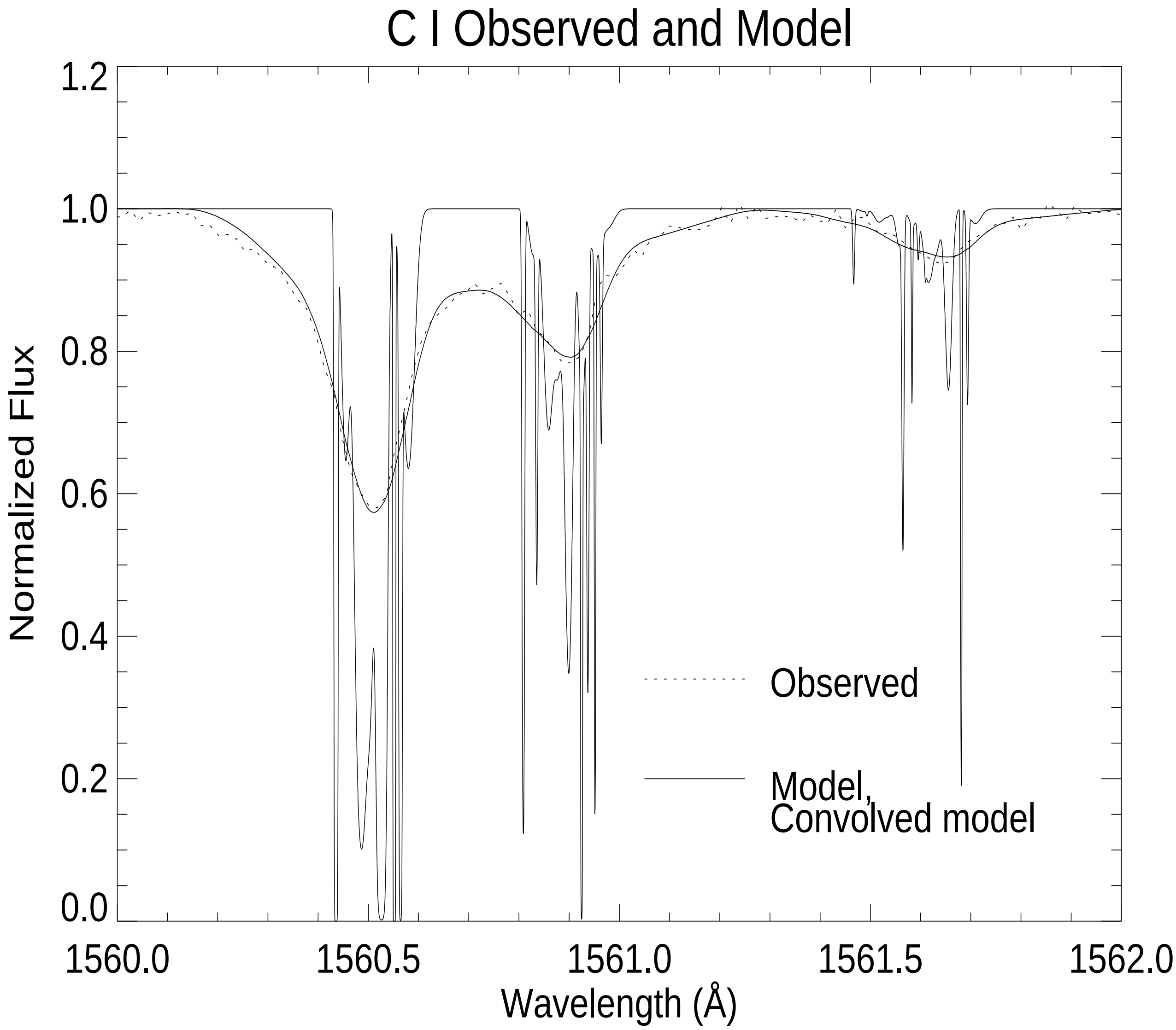
C I Observed and Model
1.2
1.0
0.8
0.6
0.4
0.2
0.0
Normalized Flux
Observed
Model,
Convolved model
1560.0
1560.5
1561.0
1561.5
1562.0
Wavelength (Å)

Figure 7

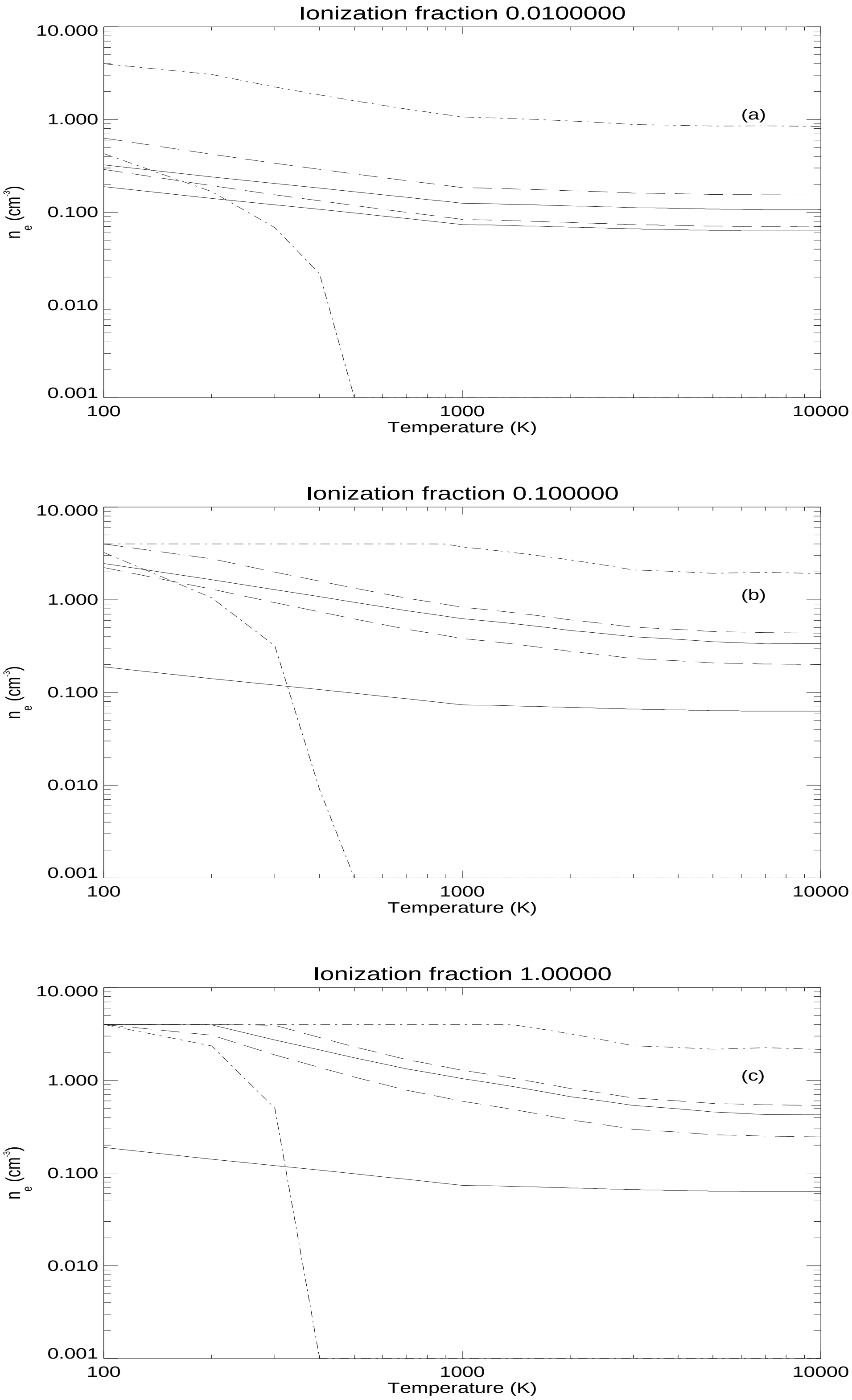
Ionization fraction 0.0100000
10.000
1.000
0.100
0.010
0.001
n_e (cm^{-3})
(a)
100
1000
10000
Temperature (K)
Ionization fraction 0.100000
(b)
Ionization fraction 1.00000
(c)